


**Non-Bloch theory for spatiotemporal photonic crystals assisted by continuum effective medium**Haozhi Ding and Kun Ding <sup>\*</sup>*Department of Physics, State Key Laboratory of Surface Physics, and Key Laboratory of Micro and Nano Photonic Structures (Ministry of Education), Fudan University, Shanghai 200438, China*

(Received 14 February 2024; accepted 23 July 2024; published 13 August 2024)

As one indispensable type of nonreciprocal mechanism, a system with temporal modulations is intrinsically open in the physical sense and inevitably non-Hermitian, but the space and time degrees of freedom are nonseparable in a large variety of circumstances, which restrains the application of the non-Bloch band theory. Here, we investigate the spatially photonic crystals (PhCs) composed of spatiotemporal modulation materials (STMs) and homogeneous media, dubbed as the STMPHC, wherein the spatial and temporal modulations are deliberately designed to be correlated. To bypass the difficulty of the spatiotemporal correlation, we first employ the effective medium theory to account for the dispersion of fundamental bands under the influence of Floquet sidebands. Based on the continuum generalized Brillouin zone condition, we then analytically give the criteria for the existence of the non-Hermitian skin effect in the STM. Assisted by developing a numerical method that embeds the plane wave expansion in the transfer matrix, we establish the non-Bloch band theory for the low-frequency Floquet bands in the STMPHCs, in which the identification of the generalized Brillouin zone is central. We finally delve into the topological properties, including non-Bloch Zak phases and non-Bloch bulk-boundary correspondence. Our work validates the idea that the effective medium assists the non-Bloch band theory applied to the STMPHCs, which delivers a prescription to broaden the horizons of non-Bloch theory.

DOI: [10.1103/PhysRevResearch.6.033167](https://doi.org/10.1103/PhysRevResearch.6.033167)**I. INTRODUCTION**

Recent increasing efforts have been devoted to a myriad of physically open systems, ranging from condensed matter to classical waves, thus leading to non-Hermitian physics [1–6]. The allure of non-Hermitian physics lies in its complex spectrum, although the non-Hermitian systems with pseudo-Hermiticity can still possess real spectra [7–12]. The complexification immediately gives rise to two intriguing spectral features unique to non-Hermitian systems, known as exceptional degeneracy and point gaps [3,4,13–16]. The former handles an abundance of geometry formed by exceptional points and corresponding properties, including higher-order exceptional lines [17,18], eigenvalue braidings [19,20], the non-Abelian conservation rule [21], and so on [3,4,13,15,22–25]. The latter indicates the nonzero eigenvalue winding numbers and further implies the wave function localization to the system boundary under open boundary conditions (OBCs), dubbed as the non-Hermitian skin effect (NHSE) [26–31]. The emergence of NHSE has led to the failure of the bulk-boundary correspondence based on the Hermitian Bloch band theory [26–28]. For restoring it, one prevailing approach is employing the generalized Brillouin zone (GBZ) to build up a comprehensive non-Bloch band theory, which works

excellently in one-dimensional (1D) systems [26,32–34]. In higher dimensions, the non-Bloch band theory and the GBZs still have the same role as in one-dimension, although how to acquire the OBC spectra and wave functions from the non-Bloch band theory for a particular class of higher-dimensional systems is still under exploration [35–41].

Aiming to investigate the non-Hermitian photonic crystals (PhCs), the fact that the non-Bloch band theory is concomitant with the NHSE requires nonreciprocal electromagnetic materials [42] since the NHSE in lattice models has been achieved mainly by using nonreciprocal hoppings [26–28]. Besides using external fields or nonlinearity, time modulation is another possibility to break reciprocity [42,43], and by using it, a plethora of schemes have then been proposed to realize a large variety of fancy phenomena, such as temporal double-slit interference [44], Fresnel drag effect [45], axion responses [46], time crystals [47–49], and so on [50–58]. As a promising nonreciprocal material, the spatiotemporal modulation materials (STMs) are excellent candidates for the component in non-Hermitian PhCs, wherein the existence of exceptional points has been revealed [59–62]. The occurrence of NHSE is then seemingly apparent, and so is the non-Bloch band theory, but establishing it in the STMs is not straightforward because of the inherently  $(d + 1)$ -dimensional problem herein ( $d$  is spatial dimensionality) [63,64]. The difference between spatiotemporal systems and purely spatial problems is at least twofold. The complexity of both problems is rooted in the boundary condition (BC) of whatever spatiality or spatiotemporality is to be considered [35,38]. However, the temporal axis possesses its own uniqueness, such as causality, which fundamentally alters the wave scattering at temporal interfaces compared with spatial boundaries [47,48,65]. It is

<sup>\*</sup>Contact author: [kunding@fudan.edu.cn](mailto:kunding@fudan.edu.cn)

Published by the American Physical Society under the terms of the [Creative Commons Attribution 4.0 International](https://creativecommons.org/licenses/by/4.0/) license. Further distribution of this work must maintain attribution to the author(s) and the published article's title, journal citation, and DOI.

more worth pointing out that most studies on spatiotemporally modulated systems nowadays deal with cases where space and time are separable or possess a uniform modulation speed in the space-time domain, certainly not fully leveraging the role of temporal degrees of freedom in non-Hermitian physics [45,46,56,59–62].

By targeting the establishment of non-Bloch band theory for the  $(1+1)$ -dimensional PhCs, we spatially stack the STM possessing a traveling-wave modulation in its permittivity and permeability with other homogeneous media, constituting the so-called STMPHCs. Firstly, we deploy the effective medium theory (EMT) to represent the fundamental Floquet band of STM influenced by the Floquet sidebands. By further using the continuum GBZ condition, we analytically work out the criterion for the existence of NHSE in STM (Sec. II). With the recipe for STM in hand and by generalizing the transfer matrix method (TMM) through embedding plane wave expansion (PWE), we establish the non-Bloch band theory for the STMPHCs by identifying the GBZ and the OBC spectra and electromagnetic fields (Sec. III). To validate the established non-Bloch band theory, we finally explore the non-Hermitian topological behaviors, including the non-Bloch Zak phase and topological edge states (TEs) in Sec. IV. The discussions and conclusions are drawn in Sec. V.

## II. NON-BLOCH PROPERTIES OF SPATIOTEMPORAL MODULATION MATERIALS

The non-Bloch band theory requires knowing the map  $f$  and its inverse  $f^{-1}$  from the complex frequency (energy) domain  $\mathbb{C}$  to the complex wave number domain  $\mathbb{C}^d$  [26,32,33,36], which is the beginning of exploring non-Bloch properties. Compared to traditional stationary models, the complex dispersion relationships arising from the interaction between wave numbers and Floquet quasifrequencies pose challenges to the study of the non-Bloch properties of STM

and the ensuing STMPHCs. The EMT, a method only valid in the long-wavelength limit, establishes the map  $f$  analytically, thereby mitigating the complexity of using non-Bloch band theory [66,67]. Aiming to utilize such analyticity and convenience, we first establish the EMT for the STM with non-Hermitian modulations in this section, which embeds the influence of Floquet sidebands in the zeroth band analytically as the effective parameters. For straightforwardly revealing the power of EMT in spatially and temporally correlated modulations, the permittivity and permeability under investigation are of a traveling-wave manner as

$$\mathbf{D}(x, t) = \varepsilon_0 \varepsilon(x, t) \mathbf{E}(x, t), \quad \mathbf{B}(x, t) = \mu_0 \mu(x, t) \mathbf{H}(x, t), \quad (1)$$

$$\varepsilon(x, t) = \varepsilon_r [1 + 2\alpha_\varepsilon \cos(gx - \Omega t + \phi_\varepsilon)], \quad (2)$$

$$\mu(x, t) = \mu_r [1 + 2\alpha_\mu \cos(gx - \Omega t + \phi_\mu)], \quad (3)$$

where  $\varepsilon_r$  ( $\mu_r$ ) represents the background permittivity (permeability),  $\alpha_\varepsilon$  ( $\alpha_\mu$ ) represents the complex modulation of permittivity (permeability),  $\phi_\varepsilon$  ( $\phi_\mu$ ) denotes the initial phase of the modulation in permittivity (permeability), and  $g$  ( $\Omega$ ) is the spatial (temporal) frequency. Figure 1(a) depicts a typical spatiotemporal modulation of material parameters and the corresponding Floquet band structure (BS) calculated by the PWE for  $E_z$  polarization is illustrated by the red lines and circles in Fig. 1(b) (see the Supplemental Material [68] for the method details; this includes Refs. [69–79]). The leading three sets of bands, namely, the fundamental order and two sidebands of order  $\pm 1$ , have been displayed in Fig. 1(b), wherein several frequency gaps are from the interaction between the fundamental bands and sidebands. If we focus on the long-wavelength limit that EMT works, namely, the bands highlighted in the black dashed box, the STM defined by Eqs. (1)–(3) can be modeled as a homogeneous bianisotropic material [45,80] (see Ref. [68] for details),

$$\begin{pmatrix} D_x \\ D_y \\ D_z \\ B_x \\ B_y \\ B_z \end{pmatrix} = \begin{pmatrix} \varepsilon_0 \varepsilon_{\text{eff},x} & 0 & 0 & 0 & 0 & 0 \\ 0 & \varepsilon_0 \varepsilon_{\text{eff},y} & 0 & 0 & 0 & +c^{-1} \xi_{\text{eff}} \\ 0 & 0 & \varepsilon_0 \varepsilon_{\text{eff},z} & 0 & -c^{-1} \xi_{\text{eff}} & 0 \\ 0 & 0 & 0 & \mu_0 \mu_{\text{eff},x} & 0 & 0 \\ 0 & 0 & -c^{-1} \xi_{\text{eff}} & 0 & \mu_0 \mu_{\text{eff},y} & 0 \\ 0 & +c^{-1} \xi_{\text{eff}} & 0 & 0 & 0 & \mu_0 \mu_{\text{eff},z} \end{pmatrix} \begin{pmatrix} E_x \\ E_y \\ E_z \\ H_x \\ H_y \\ H_z \end{pmatrix}, \quad (4)$$

where  $c = 1/\sqrt{\varepsilon_0 \mu_0}$ ,  $v = 1/\sqrt{\varepsilon_0 \mu_0 \varepsilon_r \mu_r}$ , and the effective medium parameters are

$$\varepsilon_{\text{eff},x} = \varepsilon_r, \quad \mu_{\text{eff},x} = \mu_r, \quad (5)$$

$$\varepsilon_{\text{eff},y} = \varepsilon_{\text{eff},z} = \varepsilon_r \left( 1 + \alpha_\varepsilon^2 \frac{2\Omega^2}{v^2 g^2 - \Omega^2} \right), \quad \mu_{\text{eff},y} = \mu_{\text{eff},z} = \mu_r \left( 1 + \alpha_\mu^2 \frac{2\Omega^2}{v^2 g^2 - \Omega^2} \right), \quad (6)$$

$$\xi_{\text{eff}} = \alpha_\varepsilon \alpha_\mu \frac{2cg\Omega}{v^2 g^2 - \Omega^2} \cos(\phi_\varepsilon - \phi_\mu). \quad (7)$$

The matching dispersion relation and eigenmodes for  $E_z$  polarization are

$$k_\pm = \frac{\omega}{c} \xi_{\text{eff}} \pm \frac{\omega}{c} n_{\text{eff}}, \quad \psi_\pm = \begin{pmatrix} 1 \\ \mp \frac{1}{Z_{\text{eff}}} \end{pmatrix}, \quad (8)$$

where the subscript  $\pm$  denotes the waves propagating along the  $+x$  and  $-x$  directions,  $n_{\text{eff}} = \sqrt{\varepsilon_{\text{eff},z} \mu_{\text{eff},y}}$ ,  $Z_{\text{eff}} = \sqrt{\mu_{\text{eff},y} / \varepsilon_{\text{eff},z}}$ , and  $\psi = (\sqrt{\varepsilon_0} E_z, \sqrt{\mu_0} H_y)^T$ . The dispersions by Eq. (8) are displayed by solid green lines in Fig. 1(b), and excellent agreement with the PWE is seen within the black

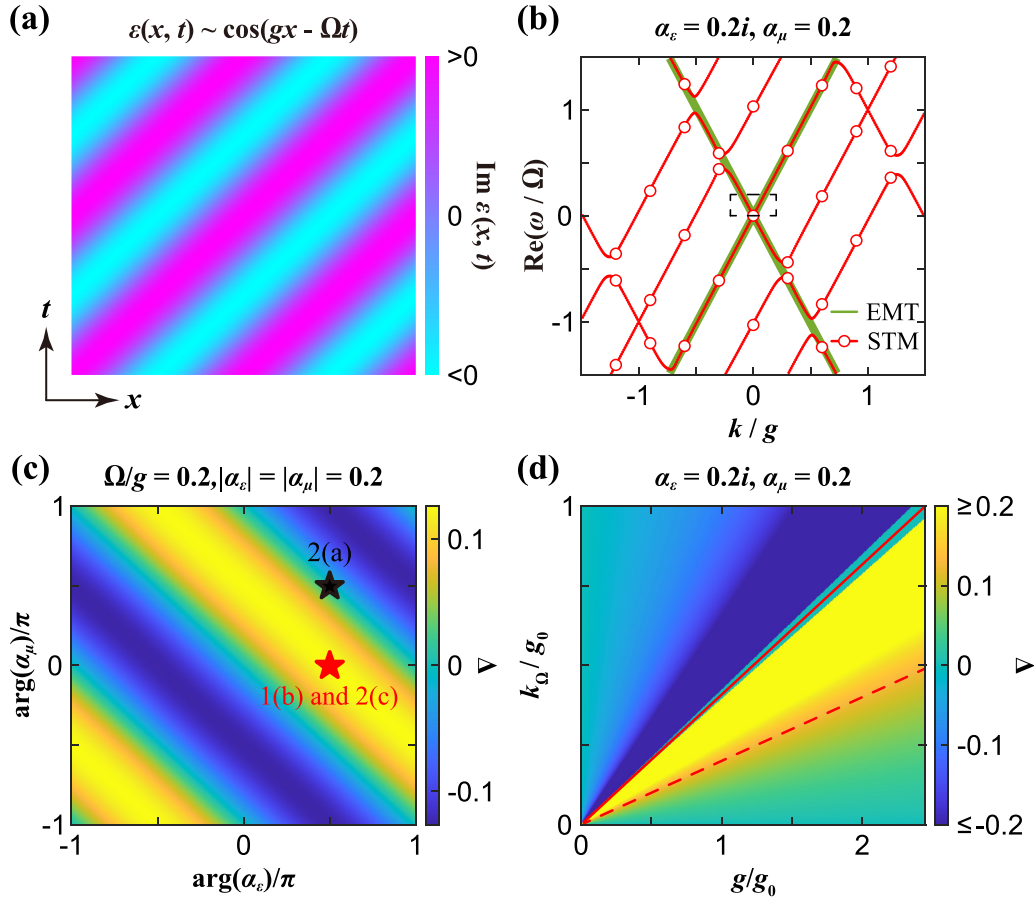


FIG. 1. (a) Schematic of the permittivity distribution in the space-time domain of an STM. (b) A typical Floquet BS for the STM (red lines and circles), wherein only real parts of the frequency are plotted. The green lines represent the EMT dispersions. (c), (d) Contour plot of  $\Delta$  in the  $\arg(\alpha_\varepsilon)$ - $\arg(\alpha_\mu)$  plane (c) and the  $g$ - $k_\Omega$  plane (d). The red pentagram in (c) and the dashed line in (d) denote the scenario of (b), and the black pentagram denotes the scenario that will be investigated in Fig. 2(a). The solid red line in (d) represents the speed of light in the background material.  $g_0$  is a parameter that accounts for the concrete physical system, facilitating the nondimensional coordinates here. Besides the parameters indicated in the figures, other parameters are  $\varepsilon_r = 6, \mu_r = 1$ , and  $\phi_\varepsilon = \phi_\mu = 0$ .

dashed box, which motivates us to utilize EMT to investigate the non-Bloch properties of STM.

When the effective medium defined by Eq. (4) is placed in a cavity (its length being  $L$ ) with its boundaries being perfect electric conductors (PECs) or perfect magnetic conductors (PMCs), the eigenfrequency and specific form of the eigenmodes under the OBC can be analytically derived (see the Supplemental Material [68] for details). From the specific forms of these OBC eigenmodes, we can see the potential emergence of NHSE. Its occurrence prevents the OBC eigenmodes from being expressed as linear combinations of traditional Bloch states. Therefore, it becomes necessary to extend the Bloch states, initially confined to the Brillouin zone (BZ), to non-Bloch states in the GBZ. Meanwhile, the OBC spectra in the thermodynamic limit ( $L \rightarrow \infty$ ) being essentially the same under various BCs also beg for the non-Bloch theory, namely, the determination of GBZ. The essence of the non-Bloch band theory is to identify the GBZ from the unit cell, so we need the non-Bloch theory for the continuum effective medium to resolve the complex wave numbers corresponding to the OBC eigenmodes and spectra. Technically speaking, the GBZ is of the same dimension as the physical one, and thus,

on top of vanishing the characteristic polynomial, another constraint is required to derive from the BCs in one dimension to determine the GBZ. The number of BCs applied at each end of the cavity is 1, and the continuum GBZ condition is then  $\text{Im } k_+ = \text{Im } k_-$  [34,75]. A simple physical interpretation of this condition is that in the thermodynamic limit, to form a standing wave, the two counterpropagating waves involved in the linear combination must exhibit the same decay behavior. By expressing  $\text{Im } k_\pm$  explicitly from Eq. (8) as

$$\text{Im } k_\pm(\omega) = \left( \frac{\omega''}{c} \xi'_{\text{eff}} + \frac{\omega'}{c} \xi''_{\text{eff}} \pm \frac{\omega''}{c} n'_{\text{eff}} \pm \frac{\omega'}{c} n''_{\text{eff}} \right), \quad (9)$$

the condition  $\text{Im } k_+(\omega^O) = \text{Im } k_-(\omega^O) = \tau(\omega^O)$  gives the following ( $\omega^O$  denotes the OBC spectrum),

$$\tau(\omega^O) = k_c(-n''_{\text{eff}} \xi'_{\text{eff}} + n'_{\text{eff}} \xi''_{\text{eff}})/n'_{\text{eff}} = k_c \Delta, \quad (10)$$

where  $k_c = \text{Re}(\omega^O)/c \in \mathbb{R}_+$  is a continuous variable in the thermodynamic limit and

$$\Delta = (-n''_{\text{eff}} \xi'_{\text{eff}} + n'_{\text{eff}} \xi''_{\text{eff}})/n'_{\text{eff}}. \quad (11)$$

The prime and double prime superscripts denote the real and imaginary parts, respectively. The quantity  $e^{-\tau}$  here plays

the same role as  $|\beta|$  in the GBZ of lattice models, where  $\beta$  describes the localization behavior of non-Bloch states; its formal definition is  $\beta = e^{ik}$  ( $k$  is the complex wave number). Equation (10), together with Eq. (8), already determines the continuum GBZ of STM for the fundamental Floquet bands. Note that we focus on the  $n'_{\text{eff}} \neq 0$  case [Eq. (11)] because  $n'_{\text{eff}} = 0$  only occurs at the transition of modulation speed from the superluminal to the subluminal region, which will be discussed later. Equation (10) not only provides the occurrence criteria for NHSE but also indicates that the sign of  $\tau(\omega^O)$  delineates the localization characteristics of NHSE. Hence, the dispersion relation [Eq. (8)] shall be solved together with the continuum GBZ condition to identify  $\tau(\omega^O)$  and the ensuing OBC spectra. As alternative evidence, the non-Bloch properties can also be examined by the dynamical degeneracy splitting (DDS) approach, which yields the same result as Eq. (11) (see the Supplemental Material [68] for details).

Since all the above considerations converge to the criterion for the emergence of NHSE, we depict in Figs. 1(c) and 1(d) the distribution of  $\Delta$  in different parameter planes. By considering  $|\alpha_{\varepsilon,\mu}| \ll 1$  in reality, resulting in  $n''_{\text{eff}} \ll n'_{\text{eff}}$  and  $n'_{\text{eff}}\xi''_{\text{eff}} \gg n''_{\text{eff}}\xi'_{\text{eff}}$ , we set  $\phi_\varepsilon = 0$  and  $\phi_\mu = 0$  throughout this work to maximize  $\xi_{\text{eff}}$ . Consequently, we investigate  $\Delta$  in two parameter planes:  $[\arg(\alpha_\varepsilon), \arg(\alpha_\mu)]$  and  $(g, \Omega)$ . Since the dominant contribution is from  $n'_{\text{eff}}\xi''_{\text{eff}}$ , the maximum value of  $\Delta$  in the  $\arg(\alpha_\varepsilon) - \arg(\alpha_\mu)$  plane occurs at  $\arg(\alpha_\varepsilon) + \arg(\alpha_\mu) = \pi/2 + n\pi$ , consistent with Fig. 1(c). This relation, which the modulation phase of  $\alpha_\varepsilon$  and  $\alpha_\mu$  should satisfy to maximize  $\Delta$ , indicates that synchronously modulating imaginary parts of  $\varepsilon$  and  $\mu$  does not imply the NHSE. In contrast, modulating real parts of  $\varepsilon$  ( $\mu$ ) and imaginary parts of  $\mu$  ( $\varepsilon$ ) simultaneously will maximize the localization of skin modes. Besides the magnitude of  $\Delta$ , Fig. 1(c) also shows its sign change by varying  $\arg(\alpha_\varepsilon)$  and  $\arg(\alpha_\mu)$ , which is seemingly straightforward from Eq. (7), whereas the sign of  $\Delta$  also flips when the modulation transits from the subluminal region ( $\Omega < vg$ ) to the superluminal one ( $\Omega > vg$ ) with all other parameters fixed. For the modulation at the red markers in Fig. 1(c), we show in Fig. 1(d) the distribution of  $\Delta$  in the  $g - \Omega$  plane. The sign change is clearly seen when the modulation goes across the speed of light ( $\Omega = vg$ ), but the effective medium near  $\Omega = vg$  becomes near zero-index material, at which Eqs. (10) and (11) should be amended (see Ref. [68] for details). Since the EMT near  $\Omega = vg$  cannot capture the essence of STM, we do not delve into the green region near the diagonal in Fig. 1(d) [81,82]. It is worth pointing out that the NHSE is absent when the modulation becomes purely spatial ( $\Omega = 0$ ) or temporal ( $g = 0$ ) since therein exists symmetry to make the spectra purely real or complex pairs, leading to the absence of point gaps [7–12,29–31].

To validate our findings, we conduct a detailed investigation of the two marked examples (red and black pentagrams) in Fig. 1(c). The Floquet BS, the OBC spectra, and a typical state are presented in Figs. 2(a) and 2(b) [Figs. 2(c) and 2(d)] for the parameters highlighted by the black (red) pentagram in Fig. 1(c). The consistency (disparity) between the periodic boundary condition (PBC) and OBC spectra in the top panel of Fig. 2(b) [Fig. 2(d)] shows the absence (appearance) of the NHSE, as demonstrated by the state (labeled by the black

arrow) shown in the bottom panel of Fig. 2(b) [Fig. 2(d)]. Moreover, the non-Bloch properties of STM calculated by PWE (markers) are reflected nicely by the EMT results (solid lines), as shown in Fig. 2. Crucially, the OBC spectra have been benchmarked by the continuum GBZ condition (see Ref. [68] for details). All demonstrate the validity of Eq. (11).

Until now, we have expounded the fundamental Floquet bands in the long-wavelength limit of the STM with their critical features under both PBC and OBC able to be captured by the EMT faithfully. More precisely, the EMT excellently models the envelope of time-averaged electromagnetic fields over the period  $2\pi/\Omega$  in the long-wavelength limit (see Ref. [68] for details). This not only illustrates the valid range of EMT but also reflects that the EMT quantifies the slow-varying components in the STMs. The fast-varying components, which the EMT cannot describe, contribute to the difference in the NHSE between STMs and EMT framework (see Ref. [68] for details). However, for the fundamental Floquet bands, the power and conciseness of EMT afford a handy way toward scrutinizing the non-Hermitian system containing the STM as one component, which will be demonstrated next.

### III. GENERALIZED BRILLOUIN ZONE OF SPATIOTEMPORAL PHOTONIC CRYSTALS

In order to corroborate the EMT recipe for the STM that can successfully embed in the composite non-Hermitian system, we now consider a spatial PhC composed of homogeneous materials and STMs, as illustrated in Fig. 3(a). The boundaries are still formed spatially and, thus, we dub the system in Fig. 3(a) the STMPhC. Let us begin with solving the PBC spectra of this STMPhC. Due to the periodicity in space-time, the modes still obey the form of Bloch-Floquet states, and the PWE method shown in Ref. [68] is then available to determine the PBC spectra, as displayed by the open stars in Fig. 3(b). Only the lower two bands are shown herein because  $\text{Re}(\omega\Lambda/2\pi c) \leq 0.6$  [equivalently,  $\text{Re}(\omega/\Omega) \leq 0.15$ ] is within the validity of EMT. This permits replacing the STM with an effective bianisotropic medium as component  $b$ , and now the PhC is constituted by two homogeneous media, referred to as an effective photonic crystal (EPhC). The corresponding EPhC results are shown in Fig. 3(b) by the solid lines, and good agreement is seen compared with the PWE method. The color of the stars and lines denotes  $\text{Im}(\omega^P)$  (the superscript  $P$  stands for the PBC case), and the correspondence from the DDS perspective indicates the NHSE for both bands propagating toward the left-hand side ( $-x$  direction) [38].

To validate the NHSE, we investigate a finite-sized STM-PhC by applying PEC BCs at both ends. The PEC here is equivalent to the Dirichlet BCs used in condensed matter. The OBC spectra generally relate to the scattering matrix, so we first formulate the TMM for the STMPhC [72,83], and the scattering matrix is then obtained recursively from the transfer matrix (see the Supplemental Material [68] for the method details). Since the TMM is numerically unstable when the wave number becomes complex, or the system size increases, we adopt TMM for the unit-cell level calculations but use the scattering matrix method (SMM) for finite-sized calculations.

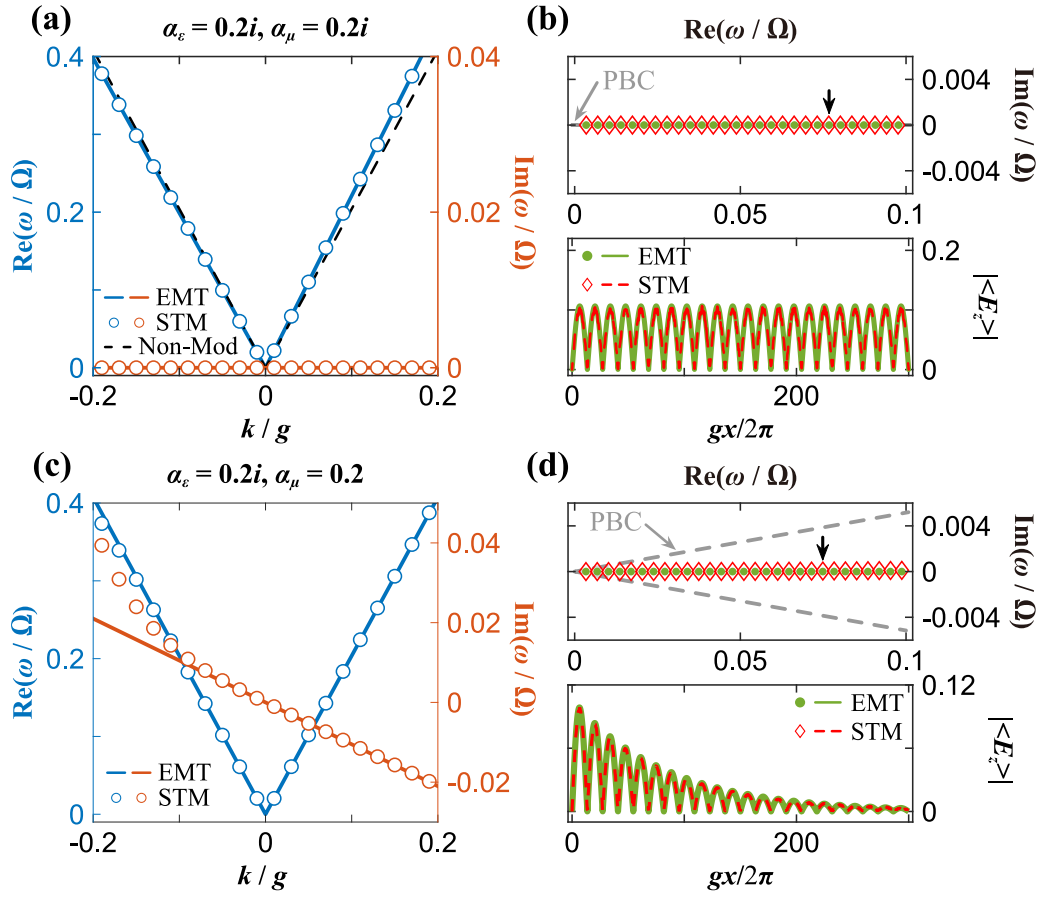


FIG. 2. (a), (c) The PBC BS in the long-wavelength limit when (a)  $\alpha_\epsilon = \alpha_\mu = 0.2i$  and (c)  $\alpha_\epsilon = 0.2i, \alpha_\mu = 0.2$ . The black dashed lines in (a) are the bands without modulations ( $\alpha_\epsilon = \alpha_\mu = 0$ ). The solid lines and open markers in (a), (c) represent the EMT and STM results, respectively. (b), (d) The OBC spectra (top) and fields (bottom) when (b)  $\alpha_\epsilon = \alpha_\mu = 0.2i$  and (d)  $\alpha_\epsilon = 0.2i, \alpha_\mu = 0.2$ . The gray dashed lines are the PBC spectra reproduced from (a), (c). The dots and lines in green and red represent the EMT and STM results, respectively. The bottom panels display the field distribution of states indicated by the black arrow. Other system parameters are  $\epsilon_r = 6, \mu_r = 1, \phi_\epsilon = \phi_\mu = 0$ , and  $\Omega/g = 0.2c$ .

The established TMM and SMM can be generalized to the STMPHCs composed of STMs with the same time-modulated frequency but possessing different spatial modulations (see Ref. [68] for details). Before obtaining the scattering matrix, we first apply the PBCs in the TMM to acquire the PBC BS [circles in Fig. 3(b)], which agrees well with both PWE and EPhC, validating the transfer matrix. By imposing the PEC BCs in the scattering matrix, we obtain the mode condition function  $g(\omega)$  (see Ref. [68] for explicit expressions), which is plotted by the color contours in Fig. 3(c). The zeros of  $g(\omega)$ , which correspond to the OBC spectra, are highlighted by the red diamond markers, and two bands and one in-gap state are seen. The  $\text{Re}(\omega^0)$  range of both bands is almost the same as the PBC one, but the  $\text{Im}(\omega^0)$  is one order of magnitude smaller than  $\text{Im}(\omega^p)$ . Such disparateness hints at the NHSE, as demonstrated by the electric field distribution (the red dashed line) in Fig. 3(d) for the bulk state marked with the black pentagram in Fig. 3(c). The skin modes apparently localize at the left-hand side boundary, confirming the previous statements. For comparison, the electric field distribution for the in-gap state is depicted in Fig. 3(e) by the red dashed line, which is localized at the right-hand side boundary. The occurrence of

NHSE and the in-gap state begs for the non-Bloch band theory because the GBZ informs the skin mode localization behavior and identifies the parametric loop on which the integral of the topological invariant performs.

As stated previously, the vanishing of the characteristic polynomial  $f(\beta, \omega) = 0$ , where  $\beta = e^{iq}$ , is inadequate to determine the GBZ, whatever  $f(\beta, \omega)$  is from the tight-binding model (TBM) or the TMM in the STMPHC. Specifically in the 1D lattice model, another constraint derived from Dirichlet BCs is known as  $|\beta_M(\omega)| = |\beta_{M+1}(\omega)|$ . This states that for the  $\omega$  in the OBC spectra, the norm of the two middle roots of  $\beta$  shall be equal when the  $2M$  roots of  $\beta$  are sorted by their moduli incrementally. Although the BCs in Fig. 3(a) are essentially Dirichlet BCs, we formally prove from the transfer matrix that the criterion for discriminating the OBC spectra in the STMPHC is still (see Ref. [68] for proof)

$$|\beta_{2l_c+1}(\omega)| = |\beta_{2l_c+2}(\omega)|. \quad (12)$$

Here,  $\beta_i$  is the  $i$ th eigenvalue of the transfer matrix. These eigenvalues are sorted in ascending order of their magnitudes as  $|\beta_1| \leq |\beta_2| \leq \dots \leq |\beta_{(4l_c+1)}| \leq |\beta_{(4l_c+2)}|$ , where  $l_c$  is the cutoff defined in the PWE (see Ref. [68] for details).

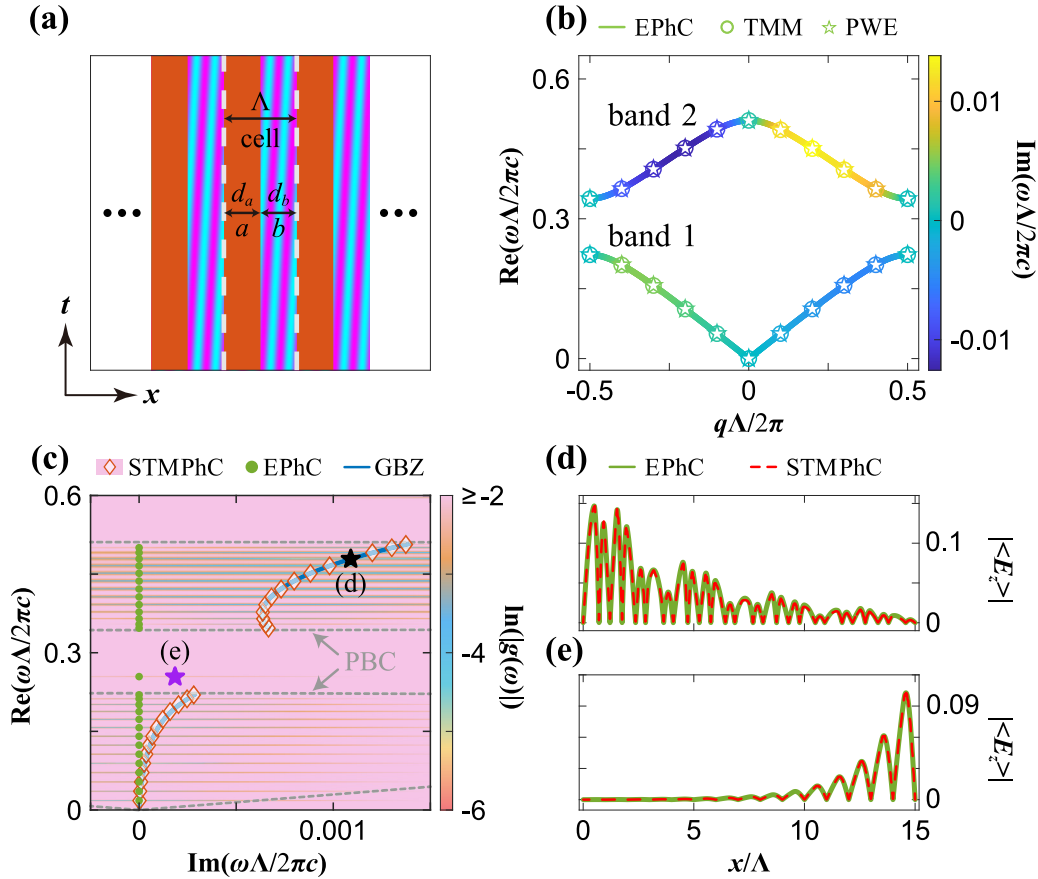


FIG. 3. (a) Schematic of a spatial PhC composed of homogeneous materials (component  $a$ ) and STMs (component  $b$ ). The unit cell is labeled herein with its lattice constant  $\Lambda = 2\pi N/g$ . (b) The PBC BS of an STMPHC with its unit cell shown in (a). The color of all these plots represents  $\text{Im}(\omega^P)$ . Solid lines, open circles, and open stars correspond to numerical results of the EPhC, TMM, and PWE, respectively. The frequency  $\text{Re}(\omega\Lambda/2\pi c) = 0.6$  here corresponds to  $\text{Re}(\omega/\Omega) = 0.15$  in Fig. 2. (c) The spectrum of a finite-sized STMPHC under PEC BCs. The color plot shows  $|g(\omega)|$  with its zeros marked by the red diamonds. The green dots and blue lines represent the results from EPhC and GBZ, respectively. The gray dashed lines are the PBC spectra reproduced from (b). The field distributions of a bulk state (black pentagram) and the TES (purple pentagram) are shown in (d,e), respectively. The green (red) lines are from the EPhC (STMPHC). The parameters of the component  $a$  are  $\varepsilon_r = \mu_r = 1$  and  $d_a/\Lambda = 0.5$  ( $N = 20$ ), while those of the component  $b$  are the same as Fig. 2(c). The number of unit cells is  $N_r = 15$ . The numerical cutoff is set to  $l_c = 2$ ,  $n_c = 60$ , and  $o_c = 100$ .

Figures 4(a) and 4(b) show the GBZ calculated by Eq. (12) for the lower two bands (blue circles). The radii of both GBZs are smaller than 1, indicating the skin modes localized at the left boundary, which is qualitatively the same as the continuum medium. We further obtain the corresponding  $\omega^O$  on the GBZs, which is depicted in Fig. 3(c) by the blue lines. The consistency between the SMM and GBZ seen in Fig. 3(c) validates Eq. (12).

To validate the EPhC description for STMPHC in the OBC, we recall the EPhC setup. The OBC spectra and field distributions calculated by the SMM are represented by green dots and lines in Figs. 3(c)–3(e), and the acquired GBZs by Eq. (12) with  $l_c = 0$  are shown by the green dashed lines in Fig. 4. Again, excellent agreement between the EPhC and STMPHC further manifests that the EMT is a faithful description and connotes the possibility of EMT-based GBZ being accessible analytically. The electromagnetic fields for  $E_z$  polarization of the EPhC satisfy

$$\hat{\mathbf{L}}\psi(x) = \frac{\omega}{c}\mathbf{K}_E(x)\psi(x), \quad (13)$$

$$\hat{\mathbf{L}} = \begin{pmatrix} 0 & i\frac{d}{dx} \\ i\frac{d}{dx} & 0 \end{pmatrix},$$

$$\mathbf{K}_E(x) = \begin{pmatrix} \varepsilon_{E,z}(x) & -\xi_E(x) \\ -\xi_E(x) & \mu_{E,y}(x) \end{pmatrix}, \quad (14)$$

$$\psi(x) = \begin{pmatrix} \sqrt{\varepsilon_0}E_z(x) \\ \sqrt{\mu_0}H_y(x) \end{pmatrix},$$

where the subscript  $E$  in  $\mathbf{K}_E$  signifies that it is the material parameter matrix describing the EPhC. The matrix components of  $\mathbf{K}_E$  are piecewise continuous functions. By considering the following transformation [66,67],

$$\psi(x) = r(x)\mathbf{D}(x)\mathbf{Q}(x), \quad (15)$$

where  $r(x) = \exp[i\int_0^x \frac{\omega}{c}\xi_E(v)dv]$ ,  $\mathbf{D}(x) = \text{Diag}[[\varepsilon_{E,z}(x)]^{-1/2}, [\mu_{E,y}(x)]^{-1/2}]$ , and  $\mathbf{Q}(x) = [Q_E(x) \quad Q_H(x)]^T$  is an auxiliary field quantity defined by Eq. (15), we

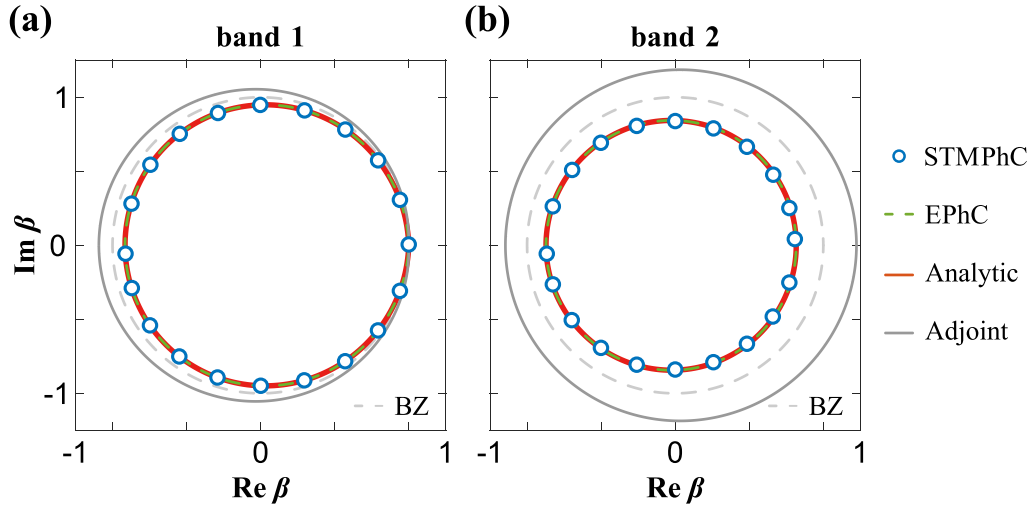


FIG. 4. The GBZs for band 1 and band 2 in Fig. 3(b) are depicted in (a), (b), respectively. The blue markers, green dashed lines, and red solid lines represent the GBZs calculated using the STMPPhC, the EPhC, and analytical methods. The solid gray line represents the adjoint GBZ, and the gray dashed line depicts the BZ.

reformulate Eq. (13) as

$$\begin{aligned} r(x)\hat{\mathbf{L}}\mathbf{D}(x)\mathbf{Q}(x) &= \left[ \frac{\omega}{c}\mathbf{K}_E(x)r(x) - [\hat{\mathbf{L}}r(x)] \right] \mathbf{D}(x)\mathbf{Q}(x) \\ &= \frac{\omega}{c}r(x)\mathbf{D}(x)^{-1}\mathbf{Q}(x). \end{aligned} \quad (16)$$

Subsequently, by introducing the operator  $\hat{\mathbf{L}}_S = \mathbf{D}(x)\hat{\mathbf{L}}\mathbf{D}(x)$ , we reorganize Eq. (16) into a more concise form as

$$\hat{\mathbf{L}}_S\mathbf{Q}(x) = \frac{\omega}{c}\mathbf{Q}(x). \quad (17)$$

The absence of  $\xi_E$  in the operator  $\hat{\mathbf{L}}_S$  indicates that the EPhC spectra are disconnected from  $\xi_E$ , and either  $Q_E(x)$  or  $Q_H(x)$  can then be used to determine the EPhC spectra. The PEC ( $E_z = 0$ ) and PMC ( $H_y = 0$ ) BCs become  $Q_E = 0$  and  $Q_H = 0$  at the boundary, which are essentially Dirichlet or Neumann BCs, depending on the  $Q_E$  or  $Q_H$  being employed. All these conclude that the OBC spectra of the EPhC [Eq. (13)] can be investigated by the operator  $\hat{\mathbf{L}}_S$  [Eq. (17)].

Concerning Fig. 3, it is crucial that  $\varepsilon_{E,z}(x)$  and  $\mu_{E,y}(x)$  are both real, thus ensuring the Hermiticity of the operator  $\hat{\mathbf{L}}_S$  under the inner product  $\langle \mathbf{Q}_1 | \mathbf{Q}_2 \rangle = \int_{x_1}^{x_2} (\mathbf{Q}_1)^\dagger \mathbf{Q}_2 dx$  [84], where the integration interval spans a unit cell (entire system) under the PBC (OBC). This explains why the OBC spectra of the EPhC lie entirely on the real axis. What is more profound is that the GBZs of the EPhC [Eq. (13)] can then be determined by Eqs. (15) and (17) analytically as

$$\beta_{n_i}(q) = \exp \left[ i \int_{\text{uc}} \frac{\omega_{n_i}^S(q)}{c} \xi_E(v) dv + iq\Lambda \right], \quad (18)$$

where  $\omega_{n_i}^S(q)$  stands for the PBC spectra of  $\hat{\mathbf{L}}_S$  with its subscript  $n_i$  (superscript  $S$ ) denoting the band index (the  $\hat{\mathbf{L}}_S$  case). Considering  $\xi_E(x)$  is a piecewise function, we can then see that  $\ln|\beta_{n_i}(q)| = -c^{-1}\omega_{n_i}^S(q)\xi_E''f_b\Lambda$ , where  $f_b = d_b/\Lambda$  is the filling ratio of the STM. When  $f_b = 0$  ( $f_b = 1$ ),  $\ln|\beta_{n_i}(q)| = 0$  [ $\ln|\beta_{n_i}(q)| = -\tau\Lambda$ ] recovers the BZ [the continuum GBZ in

Eq. (10)]. This indicates that the GBZ radius of the EPhC is determined by the filling ratio and dispersion relations together as shown by the solid red lines in Fig. 4. The excellent agreement herein reveals that Eq. (18) offers a straightforward approach to accessing the GBZ of the STMPPhC, and Eq. (15) plays exactly the same role of similarity transformation used in some intriguing TBMs [26]. Compared with Refs. [75,85], which also have utilized TMM to explore the non-Bloch properties of electromagnetic coupling materials, our method, see Eq. (15), not only provides analytical formulas for the GBZ but also eliminates the requirement of left eigenvectors when calculating topological invariants due to the Hermiticity of  $\hat{\mathbf{L}}_S$ . With such a powerful tool, we are now ready to investigate the topological properties of the STMPPhC.

#### IV. TOPOLOGICAL PROPERTIES OF SPATIOTEMPORAL PHOTONIC CRYSTALS

To examine the edge states of the STMPPhC system, we construct a domain wall formed by two STMPPhCs, as depicted in Fig. 5(a). The unit cells of both STMPPhCs are chosen to be symmetric, which will simplify the following analysis. To better leverage the analytical theory developed in the previous sections, we aim to reveal the topological properties of STMPPhCs from the EPhC approach. We set the parameters of STMPPhC2 to be the same as those that have already been investigated in Fig. 3, and Fig. 5(b) shows its non-Bloch BS, which contrasts the Bloch BS; see Fig. 3(b). With the vertical axis still showing  $\text{Re}(\omega\Lambda/2\pi c)$ , the horizontal axis uses the argument of  $\beta$  instead of  $q$ , while the line color reflects  $|\beta|$ . Such non-Bloch BS with the GBZs and the OBC spectra information contained shall be utilized when investigating the topological properties of a finite-sized system. We focus on the second non-Bloch band gap, and the non-Bloch Zak phases of the two bands below the gap are indicated therein. The non-Bloch Zak phase is calculated on the GBZ by using

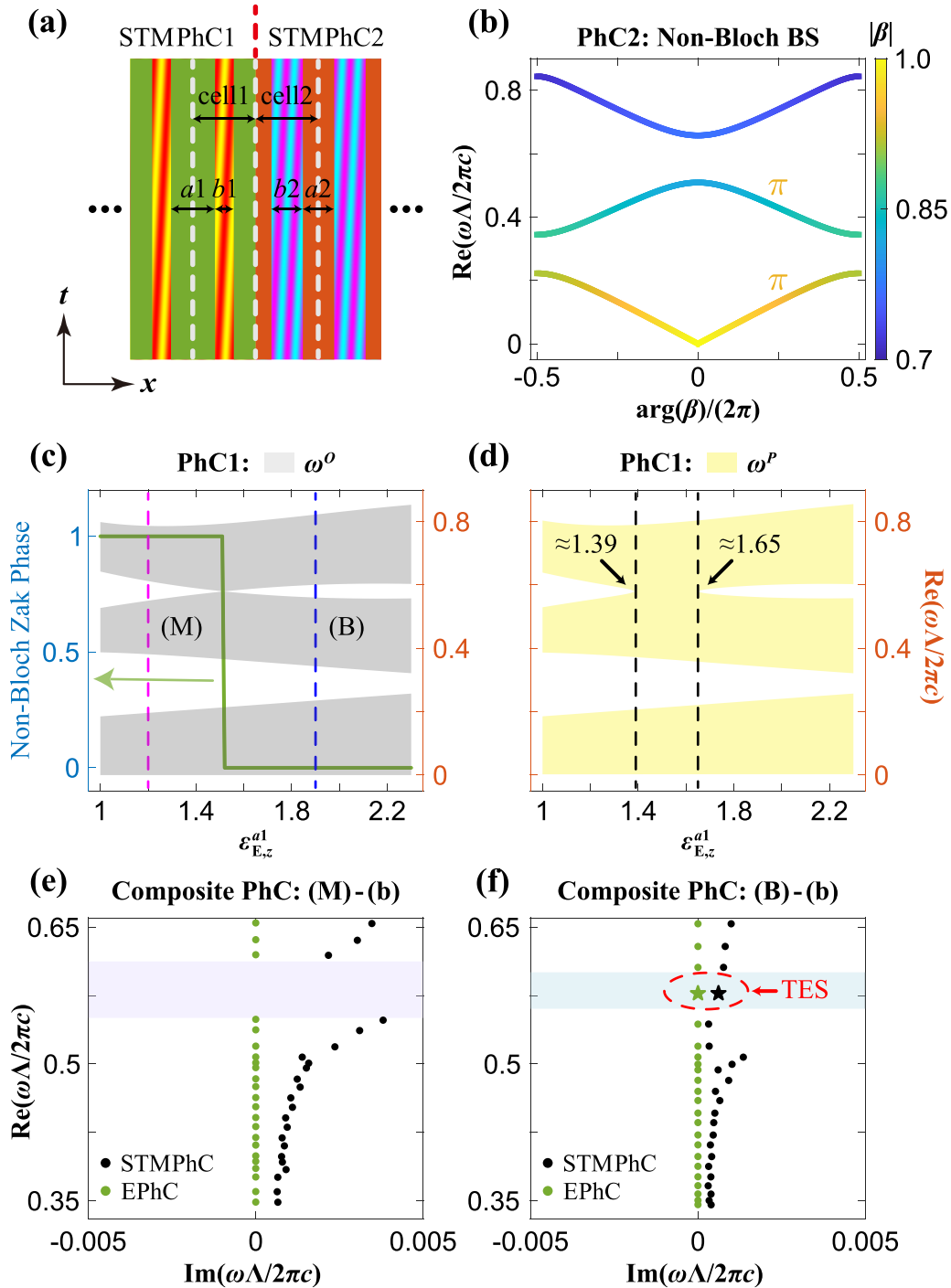


FIG. 5. (a) Schematics of a domain wall formed by two STMPPhCs. (b) The non-Bloch BS  $\text{Re}(\omega\Lambda/2\pi c) - \arg(\beta)/2\pi$  of the STMPPhC2 with the line color representing  $|\beta|$ . The non-Bloch Zak phase of each non-Bloch band is indicated nearby. The parameters herein are the same as in Fig. 3, except for the symmetric unit cell adopted here. (c) The non-Bloch Zak phase (left y axis) and the OBC spectra (right y axis) of the STMPPhC1 as a function of  $\varepsilon_{E,z}^{a1}$ . (d) The PBC spectra of the STMPPhC1 as a function of  $\varepsilon_{E,z}^{a1}$ . The parameters of the STMPPhC1 fixed in (c), (d) are  $\mu_{E,y}^{a1} = \mu_{E,y}^{b1} = 1$ ,  $d_{a1}/\Lambda = 0.7$ ,  $\alpha_\varepsilon = 0.15i$ , and  $\alpha_\mu = 0.15$ . We adjust the values of  $\varepsilon_{E,z}^{b1}$  accordingly with  $\varepsilon_{E,z}^{a1}$  to align the second non-Bloch band gap. The numerical calculations in (b–d) are performed based on the EPhC corresponding to the STMPPhC. (e), (f) The OBC spectra of the composite PhCs. The PhC in (e) [(f)] is composed of the one defined in (b) and (M) [(B)] marked in (c). The green (black) markers represent the results obtained using the EPhC (STMPPhC) setup, in which the circles (pentagrams) denote the bulk states (TESs). The purple and blue shaded regions highlight common non-Bloch band gaps of the two PhCs. The number of unit cells for both PhCs in the OBC calculations is chosen to be ten.



the following biorthogonal Berry connection,

$$\theta_{n_i}^{\text{Zak}} = \oint_{\text{GBZ}_{n_i}} d\varphi_\beta [i \langle u_{n_i, \varphi_\beta}^L | \partial_{\varphi_\beta} u_{n_i, \varphi_\beta}^R \rangle], \quad (19)$$

where  $\varphi_\beta = \arg(\beta)$ ,  $n_i$  is the band index, and  $u^R$  ( $u^L$ ) represents the periodic wave function of the non-Bloch right (left) wave function.  $u^R$  is located on the GBZ, while  $u^L$  is located on the adjoint GBZ (see the Supplemental Material [68] for the details regarding  $u^R$  and  $u^L$ ). The transformation of Eq. (15) implies that the conclusions drawn from the Hermitian PhC defined by Eq. (17) can be applied to the EPhCs, which guarantees the quantization of the non-Bloch Zak phase shown in Fig. 5(b) [79,86,87].

To make TESs occur in the second gap, we introduce the STMPHC1 by varying  $\varepsilon_{E,z}^{a1}$  and adjusting  $\varepsilon_{E,z}^{b1}$  accordingly to pin its non-Bloch band gap center at  $\frac{2\pi c}{(n_E^2 d_{a2} + n_E^2 d_{b2})}$ , where  $\{a1, a2, b1, b2\}$  denotes the regions claimed in Fig. 5(a) and  $n_E = \sqrt{\varepsilon_{E,z} \mu_{E,y}}$ . All other parameters of the STMPHC1 are fixed and claimed in the caption of Fig. 5. Figure 5(c) depicts the OBC spectra of the STMPHC1 by the gray shaded area, and the non-Bloch Zak phase of the second non-Bloch band is depicted by the solid green line. It is evident that the non-Bloch Zak phase successfully coincides with the non-Bloch band gap closure at  $\varepsilon_{E,z}^{a1} \approx 1.51$ . Its PBC spectra depicted by the light yellow shaded area are shown in Fig. 5(d) for comparison, where the second Bloch band gap is closed within  $\varepsilon_{E,z}^{a1} = 1.39$ – $1.65$ . Such inconsistency between the PBC and OBC results underscores the importance of the GBZ in non-Hermitian topology. To further illustrate, we then focus on  $\varepsilon_{E,z}^{a1} = 1.2$  (case M) and  $\varepsilon_{E,z}^{a1} = 1.9$  (case B). The non-Bloch Zak phase of the first band is  $\pi$  and will always be  $\pi$  within the chosen  $\varepsilon_{E,z}^{a1}$  range. Therefore, the TESs do not appear in the second non-Bloch band gap when  $\varepsilon_{E,z}^{a1} = 1.2$  but will emerge when  $\varepsilon_{E,z}^{a1} = 1.9$ , as demonstrated by the OBC spectra in Figs. 5(e) and 5(f). The TESs are indeed observed when  $\varepsilon_{E,z}^{a1} = 1.9$ , confirming that the non-Bloch theory based on EPhC can reflect the topological properties of STMPHCs. In addition to discussing the existence of TESs, their delocalization, a phenomenon unique to non-Hermitian systems [75–78,88], has also been demonstrated by our theory (see Ref. [68] for details). The successful employment of the GBZ established in Sec. III validates the non-Bloch BS for the STMPHC, thus providing a recipe for analyzing the fundamental Floquet bands when

they experience non-Hermiticity. From the application point of view,  $\text{Im}(\omega)$  in Fig. 5(f) is positive, and then the localization and delocalization competition unique in the non-Hermitian TES, skin modes, and their interplay potentially will give rise to various lasing scenarios [89–95].

## V. DISCUSSIONS AND CONCLUSIONS

In summary, we have established the non-Bloch band theory for the (1 + 1)-dimensional PhCs with the aid of the effective medium description for the STM. Due to the fact that the STM in the long-wavelength limit is able to be modeled by the effective medium, and also thanks to the DDS viewpoint and continuum GBZ condition, we have, firstly, analytically made clear the occurrence condition and mode profile of NHSE in the STMs. Based on such an EMT recipe, the non-Bloch band theory for the STMPHCs is then successfully formulated and verified by the TMM with multiple Floquet sidebands. As a consequence, the GBZ obtained from the non-Bloch band theory has demonstrated that it can predict the topological transition of bulk bands, restore the bulk-boundary correspondence, and realize the delocalization of TESs. The validity of our non-Bloch band theory only relies on the accuracy of effective parameters for the STM so that it can handle multiple bands and find its role in the non-Abelian Floquet system [96–98]. Regarding the generalization to  $d \geq 2$  setups, if the EMT still works, so does our prescription, which paves an alternative way to higher-dimensional spatiotemporal crystals. All powerful theoretical methods and fancy wave phenomena previously investigated at the EMT level can then be utilized to digest the non-Hermitian physics in higher-dimensional Floquet systems [96,98,99]. The holistic view of the  $(d + 1)$ -dimensional problem requires further investigation because the space-time symmetry and spatiotemporal boundaries shall be considered together [63,64], but the numerical method established here provides one scheme to cope with both the spectra and wave functions.

## ACKNOWLEDGMENTS

We thank Dr. Jing Lin and Dr. Mengying Hu for the helpful discussions. This work is supported by the National Key R&D Program of China (Grants No. 2022YFA1404701 and No. 2022YFA1404500) and the National Natural Science Foundation of China (Grants No. 12174072 and No. 2021hwyq05).

- 
- [1] L. Feng, R. El-Ganainy, and L. Ge, Non-Hermitian photonics based on parity-time symmetry, *Nat. Photon.* **11**, 752 (2017).
  - [2] R. El-Ganainy, K. G. Makris, M. Khajavikhan, Z. H. Musslimani, S. Rotter, and D. N. Christodoulides, Non-Hermitian physics and  $\mathcal{PT}$  symmetry, *Nat. Phys.* **14**, 11 (2018).
  - [3] Y. Ashida, Z. Gong, and M. Ueda, Non-Hermitian physics, *Adv. Phys.* **69**, 249 (2020).
  - [4] E. J. Bergholtz, J. C. Budich, and F. K. Kunst, Exceptional topology of non-Hermitian systems, *Rev. Mod. Phys.* **93**, 015005 (2021).
  - [5] K. Ding, C. Fang, and G. Ma, Non-Hermitian topology and exceptional-point geometries, *Nat. Rev. Phys.* **4**, 745 (2022).
  - [6] N. Okuma and M. Sato, Non-Hermitian topological phenomena: A review, *Annu. Rev. Condens. Matter Phys.* **14**, 83 (2023).
  - [7] C. M. Bender and S. Boettcher, Real spectra in non-Hermitian hamiltonians having  $\mathcal{PT}$  symmetry, *Phys. Rev. Lett.* **80**, 5243 (1998).
  - [8] C. M. Bender, D. C. Brody, and H. F. Jones, Complex extension of quantum mechanics, *Phys. Rev. Lett.* **89**, 270401 (2002).
  - [9] C. M. Bender, M. V. Berry, and A. Mandilara, Generalized  $\mathcal{PT}$  symmetry and real spectra, *J. Phys. A* **35**, L467 (2002).
  - [10] A. Mostafazadeh, Pseudo-Hermiticity versus  $\mathcal{PT}$  symmetry: The necessary condition for the reality of the spectrum

- of a non-Hermitian Hamiltonian, *J. Math. Phys.* **43**, 205 (2002).
- [11] A. Mostafazadeh, Pseudo-Hermiticity versus  $\mathcal{PT}$ -symmetry. II. A complete characterization of non-Hermitian Hamiltonians with a real spectrum, *J. Math. Phys.* **43**, 2814 (2002).
- [12] A. Mostafazadeh, Pseudo-Hermiticity versus  $\mathcal{PT}$ -symmetry III: Equivalence of pseudo-Hermiticity and the presence of antilinear symmetries, *J. Math. Phys.* **43**, 3944 (2002).
- [13] K. Ding, Z. Q. Zhang, and C. T. Chan, Coalescence of exceptional points and phase diagrams for one-dimensional  $\mathcal{PT}$ -symmetric photonic crystals, *Phys. Rev. B* **92**, 235310 (2015).
- [14] H. Shen, B. Zhen, and L. Fu, Topological band theory for non-Hermitian Hamiltonians, *Phys. Rev. Lett.* **120**, 146402 (2018).
- [15] X. Cui, K. Ding, J.-W. Dong, and C. T. Chan, Exceptional points and their coalescence of  $\mathcal{PT}$ -symmetric interface states in photonic crystals, *Phys. Rev. B* **100**, 115412 (2019).
- [16] K. Kawabata, K. Shiozaki, M. Ueda, and M. Sato, Symmetry and topology in non-Hermitian physics, *Phys. Rev. X* **9**, 041015 (2019).
- [17] J. Hu, R.-Y. Zhang, Y. Wang, X. Ouyang, Y. Zhu, H. Jia, and C. T. Chan, Non-Hermitian swallowtail catastrophe revealing transitions among diverse topological singularities, *Nat. Phys.* **19**, 1098 (2023).
- [18] W. Tang, K. Ding, and G. Ma, Realization and topological properties of third-order exceptional lines embedded in exceptional surfaces, *Nat. Commun.* **14**, 6660 (2023).
- [19] K. Wang, A. Dutt, C. C. Wojcik, and S. Fan, Topological complex-energy braiding of non-Hermitian bands, *Nature (London)* **598**, 59 (2021).
- [20] Y. S. S. Patil, J. Höller, P. A. Henry, C. Guria, Y. Zhang, L. Jiang, N. Kralj, N. Read, and J. G. E. Harris, Measuring the knot of non-Hermitian degeneracies and non-commuting braids, *Nature (London)* **607**, 271 (2022).
- [21] C.-X. Guo, S. Chen, K. Ding, and H. Hu, Exceptional non-Abelian topology in multiband non-Hermitian systems, *Phys. Rev. Lett.* **130**, 157201 (2023).
- [22] K. Ding, G. Ma, M. Xiao, Z. Q. Zhang, and C. T. Chan, Emergence, coalescence, and topological properties of multiple exceptional points and their experimental realization, *Phys. Rev. X* **6**, 021007 (2016).
- [23] W. Chen, Ş. Kaya Özdemir, G. Zhao, J. Wiersig, and L. Yang, Exceptional points enhance sensing in an optical microcavity, *Nature (London)* **548**, 192 (2017).
- [24] K. Ding, G. Ma, Z. Q. Zhang, and C. T. Chan, Experimental demonstration of an anisotropic exceptional point, *Phys. Rev. Lett.* **121**, 085702 (2018).
- [25] W. Tang, X. Jiang, K. Ding, Y.-X. Xiao, Z.-Q. Zhang, C. T. Chan, and G. Ma, Exceptional nexus with a hybrid topological invariant, *Science* **370**, 1077 (2020).
- [26] S. Yao and Z. Wang, Edge states and topological invariants of non-Hermitian systems, *Phys. Rev. Lett.* **121**, 086803 (2018).
- [27] F. K. Kunst, E. Edvardsson, J. C. Budich, and E. J. Bergholtz, Biorthogonal bulk-boundary correspondence in non-Hermitian systems, *Phys. Rev. Lett.* **121**, 026808 (2018).
- [28] T. Helbig, T. Hofmann, S. Imhof, M. Abdelghany, T. Kiessling, L. W. Molenkamp, C. H. Lee, A. Szameit, M. Greiter, and R. Thomale, Generalized bulk-boundary correspondence in non-Hermitian topoelectrical circuits, *Nat. Phys.* **16**, 747 (2020).
- [29] D. S. Borgnia, A. J. Kruchkov, and R.-J. Slager, Non-Hermitian boundary modes and topology, *Phys. Rev. Lett.* **124**, 056802 (2020).
- [30] K. Zhang, Z. Yang, and C. Fang, Correspondence between winding numbers and skin modes in non-Hermitian systems, *Phys. Rev. Lett.* **125**, 126402 (2020).
- [31] N. Okuma, K. Kawabata, K. Shiozaki, and M. Sato, Topological origin of non-Hermitian skin effects, *Phys. Rev. Lett.* **124**, 086801 (2020).
- [32] K. Yokomizo and S. Murakami, Non-Bloch band theory of non-Hermitian systems, *Phys. Rev. Lett.* **123**, 066404 (2019).
- [33] Z. Yang, K. Zhang, C. Fang, and J. Hu, Non-Hermitian bulk-boundary correspondence and auxiliary generalized Brillouin zone theory, *Phys. Rev. Lett.* **125**, 226402 (2020).
- [34] Y.-M. Hu, Y.-Q. Huang, W.-T. Xue, and Z. Wang, Non-Bloch band theory for non-Hermitian continuum systems, [arXiv:2310.08572](https://arxiv.org/abs/2310.08572).
- [35] K. Zhang, Z. Yang, and C. Fang, Universal non-Hermitian skin effect in two and higher dimensions, *Nat. Commun.* **13**, 2496 (2022).
- [36] H.-Y. Wang, F. Song, and Z. Wang, Amoeba formulation of non-Bloch band theory in arbitrary dimensions, *Phys. Rev. X* **14**, 021011 (2024).
- [37] K. Yokomizo and S. Murakami, Non-Bloch bands in two-dimensional non-Hermitian systems, *Phys. Rev. B* **107**, 195112 (2023).
- [38] K. Zhang, C. Fang, and Z. Yang, Dynamical degeneracy splitting and directional invisibility in non-Hermitian systems, *Phys. Rev. Lett.* **131**, 036402 (2023).
- [39] K. Zhang, Z. Yang, and K. Sun, Edge theory of non-Hermitian skin modes in higher dimensions, *Phys. Rev. B* **109**, 165127 (2024).
- [40] Z. Xu, B. Pang, K. Zhang, and Z. Yang, Two-dimensional asymptotic generalized Brillouin zone theory, [arXiv:2311.16868v2](https://arxiv.org/abs/2311.16868v2).
- [41] W. Wang, M. Hu, X. Wang, G. Ma, and K. Ding, Experimental realization of geometry-dependent skin effect in a reciprocal two-dimensional lattice, *Phys. Rev. Lett.* **131**, 207201 (2023).
- [42] J. A. Kong, *Electromagnetic Wave Theory* (Wiley InterScience, Hoboken, NJ, 1986).
- [43] C. Caloz, A. Alù, S. Tretyakov, D. Sounas, K. Achouri, and Z.-L. Deck-Léger, Electromagnetic nonreciprocity, *Phys. Rev. Appl.* **10**, 047001 (2018).
- [44] R. Tirole, S. Vezzoli, E. Galiffi, I. Robertson, D. Maurice, B. Tilmann, S. A. Maier, J. B. Pendry, and R. Sapienza, Double-slit time diffraction at optical frequencies, *Nat. Phys.* **19**, 999 (2023).
- [45] P. A. Huidobro, E. Galiffi, S. Guenneau, R. V. Craster, and J. B. Pendry, Fresnel drag in space-time-modulated metamaterials, *Proc. Natl. Acad. Sci. USA* **116**, 24943 (2019).
- [46] F. R. Prudêncio and M. G. Silveirinha, Synthetic axion response with space-time crystals, *Phys. Rev. Appl.* **19**, 024031 (2023).
- [47] E. Lustig, Y. Sharabi, and M. Segev, Topological aspects of photonic time crystals, *Optica* **5**, 1390 (2018).
- [48] M. Lyubarov, Y. Lumer, A. Dikopoltsev, E. Lustig, Y. Sharabi, and M. Segev, Amplified emission and lasing in photonic time crystals, *Science* **377**, 425 (2022).
- [49] P. Kongkhambut, J. Skulte, L. Mathey, J. G. Cosme, A. Hemmerich, and H. Keßler, Observation of a continuous time crystal, *Science* **377**, 670 (2022).

- [50] C. Caloz and Z. L. Deck-Léger, Spacetime metamaterials—Part I: General concepts, *IEEE Trans. Antennas Propag.* **68**, 1569 (2020).
- [51] V. Pacheco-Peña and N. Engheta, Antireflection temporal coatings, *Optica* **7**, 323 (2020).
- [52] V. Pacheco-Peña and N. Engheta, Temporal equivalent of the Brewster angle, *Phys. Rev. B* **104**, 214308 (2021).
- [53] C. Guo, M. Xiao, M. Orenstein, and S. Fan, Structured 3D linear space-time light bullets by nonlocal nanophotonics, *Light Sci. Appl.* **10**, 160 (2021).
- [54] G.-B. Wu, J. Y. Dai, Q. Cheng, T. J. Cui, and C. H. Chan, Sideband-free space-time-coding metasurface antennas, *Nat. Electron.* **5**, 808 (2022).
- [55] J. Park, H. Cho, S. Lee, K. Lee, K. Lee, H. C. Park, J.-W. Ryu, N. Park, S. Jeon, and B. Min, Revealing non-Hermitian band structure of photonic Floquet media, *Sci. Adv.* **8**, eabo6220 (2022).
- [56] F. R. Prudêncio and M. G. Silveirinha, Replicating physical motion with Minkowskian isorefractive spacetime crystals, *Nanophotonics* **12**, 3007 (2023).
- [57] L. Zhou and D.-J. Zhang, Non-Hermitian Floquet topological matter—a review, *Entropy* **25**, 1401 (2023).
- [58] Z. Dong, X. Chen, and L. Yuan, Spatiotemporal coupled-mode equations for arbitrary pulse transformation, *Phys. Rev. Res.* **5**, 043150 (2023).
- [59] N. Chamanara, Z.-L. Deck-Léger, C. Caloz, and D. Kalluri, Unusual electromagnetic modes in space-time-modulated dispersion-engineered media, *Phys. Rev. A* **97**, 063829 (2018).
- [60] N. Wang, Z.-Q. Zhang, and C. T. Chan, Photonic Floquet media with a complex time-periodic permittivity, *Phys. Rev. B* **98**, 085142 (2018).
- [61] Y. Sharabi, A. Dikopoltsev, E. Lustig, Y. Lumer, and M. Segev, Spatiotemporal photonic crystals, *Optica* **9**, 585 (2022).
- [62] M. Moghaddasadeh, M. A. Attarzadeh, A. Aref, and M. Nouh, Complex spatiotemporal modulations and non-Hermitian degeneracies in  $\mathcal{PT}$ -symmetric phononic materials, *Phys. Rev. Appl.* **18**, 044013 (2022).
- [63] S. Xu and C. Wu, Space-time crystal and space-time group, *Phys. Rev. Lett.* **120**, 096401 (2018).
- [64] Q. Gao and Q. Niu, Floquet-Bloch oscillations and intraband Zener tunneling in an oblique spacetime crystal, *Phys. Rev. Lett.* **127**, 036401 (2021).
- [65] H. Moussa, G. Xu, S. Yin, E. Galiffi, Y. Ra'di, and A. Alù, Observation of temporal reflection and broadband frequency translation at photonic time interfaces, *Nat. Phys.* **19**, 863 (2023).
- [66] K. Yokomizo, T. Yoda, and S. Murakami, Non-Hermitian waves in a continuous periodic model and application to photonic crystals, *Phys. Rev. Res.* **4**, 023089 (2022).
- [67] T. Yoda, Y. Moritake, K. Takata, K. Yokomizo, S. Murakami, and M. Notomi, Optical non-Hermitian skin effect in two-dimensional uniform media, [arXiv:2303.05185](https://arxiv.org/abs/2303.05185).
- [68] See Supplemental Material at <http://link.aps.org/supplemental/10.1103/PhysRevResearch.6.033167> for detailed discussions on plane wave expansion, effective medium theory, boundary conditions, dynamical degeneracy splitting, transfer matrix, non-Bloch band theory, and topological properties, which include Refs. [32,38,42,43,45,69–79].
- [69] M. Davanco, Y. Urzhumov, and G. Shvets, The complex Bloch bands of a 2D plasmonic crystal displaying isotropic negative refraction, *Opt. Express* **15**, 9681 (2007).
- [70] C. Fietz, Y. Urzhumov, and G. Shvets, Complex  $k$  band diagrams of 3D metamaterial/photonic crystals, *Opt. Express* **19**, 19027 (2011).
- [71] J. H. D. Rivero, L. Feng, and L. Ge, Imaginary gauge transformation in momentum space and Dirac exceptional point, *Phys. Rev. Lett.* **129**, 243901 (2022).
- [72] A. Yariv and P. A. Yeh, *Optical Waves in Crystals: Propagation and Control of Laser Radiation* (Wiley, New York, 1983).
- [73] L. Li, Formulation and comparison of two recursive matrix algorithms for modeling layered diffraction gratings, *J. Opt. Soc. Am. A* **13**, 1024 (1996).
- [74] G. B. Arfken, H. J. Weber, and F. E. Harris, in *Mathematical Methods for Physicists (Seventh Edition)*, edited by G. B. Arfken, H. J. Weber, and F. E. Harris (Academic Press, Boston, 2013), p. 381.
- [75] Q. Yan, H. Chen, and Y. Yang, Non-Hermitian skin effect and delocalized edge states in photonic crystals with anomalous parity-time symmetry, *Prog. Electromagn. Res.* **172**, 33 (2021).
- [76] W. Zhu, W. X. Teo, L. Li, and J. Gong, Delocalization of topological edge states, *Phys. Rev. B* **103**, 195414 (2021).
- [77] W. Wang, X. Wang, and G. Ma, Non-Hermitian morphing of topological modes, *Nature (London)* **608**, 50 (2022).
- [78] W. Wang, X. Wang, and G. Ma, Extended state in a localized continuum, *Phys. Rev. Lett.* **129**, 264301 (2022).
- [79] M. Xiao, Z. Q. Zhang, and C. T. Chan, Surface impedance and bulk band geometric phases in one-dimensional systems, *Phys. Rev. X* **4**, 021017 (2014).
- [80] P. A. Huidobro, M. G. Silveirinha, E. Galiffi, and J. B. Pendry, Homogenization theory of space-time metamaterials, *Phys. Rev. Appl.* **16**, 014044 (2021).
- [81] J. B. Pendry, E. Galiffi, and P. A. Huidobro, Gain in time-dependent media—a new mechanism, *J. Opt. Soc. Am. B* **38**, 3360 (2021).
- [82] J. B. Pendry, E. Galiffi, and P. A. Huidobro, Photon conservation in trans-luminal metamaterials, *Optica* **9**, 724 (2022).
- [83] E. Galiffi, P. A. Huidobro, and J. B. Pendry, Broadband non-reciprocal amplification in luminal metamaterials, *Phys. Rev. Lett.* **123**, 206101 (2019).
- [84] K. Sakoda, *Optical Properties of Photonic Crystals* (Springer, Berlin, 2004).
- [85] K. Yokomizo, T. Yoda, and Y. Ashida, Non-Bloch band theory of generalized eigenvalue problems, *Phys. Rev. B* **109**, 115115 (2024).
- [86] J. Zak, Berry's phase for energy bands in solids, *Phys. Rev. Lett.* **62**, 2747 (1989).
- [87] D. Vanderbilt, *Berry Phases in Electronic Structure Theory: Electric Polarization, Orbital Magnetization and Topological Insulators* (Cambridge University Press, Cambridge, 2018).
- [88] A. M. Jazayeri, Fixed points on band structures of non-Hermitian models: Extended states in the bandgap and ideal superluminal tunneling, *Phys. Rev. B* **107**, 144302 (2023).
- [89] P. St-Jean, V. Goblot, E. Galopin, A. Lemaître, T. Ozawa, L. Le Gratiet, I. Sagnes, J. Bloch, and A. Amo, Author Correction: Lasing in topological edge states of a one-dimensional lattice, *Nat. Photon.* **15**, 862 (2021).

- [90] M. A. Bandres, S. Wittek, G. Harari, M. Parto, J. Ren, M. Segev, D. N. Christodoulides, and M. Khajavikhan, Topological insulator laser: Experiments, *Science* **359**, eaar4005 (2018).
- [91] M. Parto, S. Wittek, H. Hodaei, G. Harari, M. A. Bandres, J. Ren, M. C. Rechtsman, M. Segev, D. N. Christodoulides, and M. Khajavikhan, Edge-mode lasing in 1D topological active arrays, *Phys. Rev. Lett.* **120**, 113901 (2018).
- [92] C. Han, M. Lee, S. Callard, C. Seassal, and H. Jeon, Lasing at topological edge states in a photonic crystal  $L3$  nanocavity dimer array, *Light Sci. Appl.* **8**, 40 (2019).
- [93] Z.-Q. Yang, Z.-K. Shao, H.-Z. Chen, X.-R. Mao, and R.-M. Ma, Spin-momentum-locked edge mode for topological vortex lasing, *Phys. Rev. Lett.* **125**, 013903 (2020).
- [94] H.-R. Kim, M.-S. Hwang, D. Smirnova, K.-Y. Jeong, Y. Kivshar, and H.-G. Park, Multipolar lasing modes from topological corner states, *Nat. Commun.* **11**, 5758 (2020).
- [95] Y.-G. Sang, J.-Y. Lu, Y.-H. Ouyang, H.-Y. Luan, J.-H. Wu, J.-Y. Li, and R.-M. Ma, Topological polarization singular lasing with highly efficient radiation channel, *Nat. Commun.* **13**, 6485 (2022).
- [96] R.-J. Slager, A. Bouhon, and F. N. Ünal, Non-Abelian Floquet braiding and anomalous Dirac string phase in periodically driven systems, *Nat. Commun.* **15**, 1144 (2024).
- [97] T. Li and H. Hu, Floquet non-Abelian topological insulator and multifold bulk-edge correspondence, *Nat. Commun.* **14**, 6418 (2023).
- [98] R.-J. Slager, A. Bouhon, and F. N. Ünal, Comment on “Floquet non-Abelian topological insulator and multifold bulk-edge correspondence”, [arXiv:2310.12782v2](https://arxiv.org/abs/2310.12782v2).
- [99] K.-M. Kim and M. J. Park, Disorder-driven phase transition in the second-order non-Hermitian skin effect, *Phys. Rev. B* **104**, L121101 (2021).